A pH-Driven active ingredient-loaded nanomedicine for effective rheumatoid arthritis therapy by combining with photothermal therapy

Shengtao Hu, Ye Lin, Chunyi Tong, Hong Huang, Ouyang Yi, Zongshun Dai, Zhaoli Su, Bin Liu & Xiong Cai

Taylor & Francis
Taylor & Francis Group

Check for updates

ORIGINAL ARTICLE

A pH-Driven active ingredient-loaded nanomedicine for effective rheumatoid arthritis therapy by combining with photothermal therapy

Shengtao Hu[a]*, Ye Lin[a]*, Chunyi Tong[b], Hong Huang[a], Ouyang Yi[a], Zongshun Dai[a], Zhaoli Su[a], Bin Liu[b] and Xiong Cai[a]

[a]Institute of Innovation and Applied Research in Chinese Medicine and Department of Rheumatology of The First Hospital, Hunan University of Chinese Medicine, Changsha, Hunan, China; [b]College of Biology, Hunan University, Changsha, Hunan, China

ABSTRACT

Rheumatoid arthritis (RA) is a systemic autoimmune disease characterised by inflammatory micro-environ-ments in the joints. Active ingredient (IND), a conventional nonsteroidal anti-inflammatory drug (NSAID), has been used for the therapy of RA. However, the poor solubility and serious side effects of oral administration of IND significantly limit its efficacy. In this study, we have synthesized biomimetic IND-loaded Prussian blue (PB) nanoparticles (IND@PB@M@HA) with hyaluronic acid (HA) modification for increasing the solubility and targeting the ability of IND to the inflamed joints. The application of hybrid cell membranes on the NPs endowed immune escape of IND@PB@M@HA NPs, which accordingly extended the circulation time in the blood. *In vitro* assay demonstrated that the combination of nanomedicine and photothermal therapy produced a powerful anti-inflammatory effect by reducing the levels of inflammatory factors and cell viabil-ity of activated macrophages and NPs possessed obvious pH-responsiveness. *In vivo* assay demonstrated that the nanomedicine for synergistic photothermal therapy exhibited desirable pharmacodynamics and pharmacokinetic properties at ultra-low drug dosage in a rat model of adjuvant-induced arthritis, which was confirmed by inflammatory suppression, bone erosion remission, and negligible adverse effects. In summary, the proposed nanomedicine has the potential role for targeted anti-inflammatory therapy of RA.

Introduction

As a highly prevalent chronic autoimmune disease, rheumatoid arthritis (RA) displays pathological features including synovial lin-ing hyperplasia, autoantibody production, inflammatory cell infil-tration (such as activated macrophages), cartilage destruction and bone erosion, eventually pannus production or irreversible joints damage [1]. Statistical data have revealed that approximately 0.5–1% of the global population are suffered from RA, where women are 3-fold more likely to be afflicted with RA than men [2]. Considering that the inflammatory cascade is the primary cause of the development of RA, non-steroidal anti-inflammatory drugs (NSAIDs) have been widely used for RA therapy. Among them, active ingredient (IND) can effectively reduce swelling and stiff-ness of joints by blocking cyclooxygenases and prostaglandin pro-duction [3]; however, long-term oral administration of IND can cause significant cardiovascular and gastrointestinal toxicity [4], which eventually result in the usage termination in 37.8% of patients [5]. In addition, both the anti-inflammatory and immuno-suppressive drugs on clinical applications differentially involved non-specific immune cell suppression and off-target toxicity [6].

With the rapid development of nanotechnology and the encouragement of advantageous properties offered by nanomate-rials [7], nanomedicine has become increasingly popular in the treatment of RA. Photothermal therapy (PTT) is an emerging technology that increases tissue locally temperature through dir-ectly absorbing near-infra-red (NIR) light and transforming the energy, thereby generating hyperthermia effects, inhibiting abnor-mal tissue growth or pannus formation, and causing cell apoptosis [8]. For RA treatment, NIR light with a particular penetration depth can penetrate the small inflamed joints that guarantee the prac-tical application of nanomaterials based PTT [9]. Until now, Prussian blue (PB) nanoparticles (NPs) with a hollow mesoporous structure have been used to deliver drugs and enzymes to achieve high drug loading therapy [10]. Meanwhile, PB NPs with high pho-tothermal conversion efficiency showed the distinct RA therapy by inducing higher temperature during the photothermal therapy and generated a better inflammatory inhibition effect [11]. Moreover, PB NPs exhibited strong scavenging reactive oxygen species (ROS) ability to treat abnormal cells or tissues [12]. In add-ition, the loaded therapeutic drug can be released at the targeted site in a controlled-release manner under the stimulation of pH [13], and/or light [8] and so on. Considering we have developed a chemo-/photothermal strategy for cancer therapy using PB as a drug carrier and photosensitizer in previous work and the advan-tages of PB NPs [14], it is highly promising to construct a multi-functional nanosystem of IND loaded PB NPs (IND@PB NPs) to achieve efficient RA therapy by combining the anti-inflammatory effect of IND and the photothermal ability of PB NPs.

The cell membranes coating technology provides nanoparticles with a natural surface to avoid immune clearance. Meanwhile, cell membranes coating can extend circulation half-life while retaining their inherent physicochemical properties [15,16]. Recently, the red blood cell membranes were reported to efficiently improve the ability of nanomaterials to evade the immune system due to the presence of special surface proteins including CD47 [17], while macrophage membrane-coated nanoparticles demonstrated high targeted delivery or therapeutic efficacy in RA [18]. Proteome analysis suggested that NPs can adhere to the endothelium associated with RA through CD44 [19]. CD44 is an adhesion receptor highly expressed in macrophages, fibroblasts, and lining cells under an inflammatory environment. Hyaluronic acid (HA)-modified solid lipid nanoparticles have been used for targeted therapy of RA through endocytosis mediated by the CD44 receptor [20]. Therefore, we designed a new nano complex possessing several advantages of effective immune escape, cell targeting as well as joint penetration and controllable drug release was designed. IND@PB NPs were coated with hybrid membranes (denoted as IND@PB@M) and HA (denoted as IND@PB@M@HA) to prepare IND@PB@M@HA NPs (Figure 1a). The nanomedicine was expected to actively target the cells of inflamed joints by recognising CD44 molecules of the macrophages. In addition, as the inflamed joints are characterised by an acid environment with pH approximately ranging from 5.0 to 6.0 [21], the release of drug from nanomedicine under an acid environment and laser irradiation efficiently killed the pathological macrophages and synovial cells to exert therapeutic effects (Figure 1b). Given these properties, we
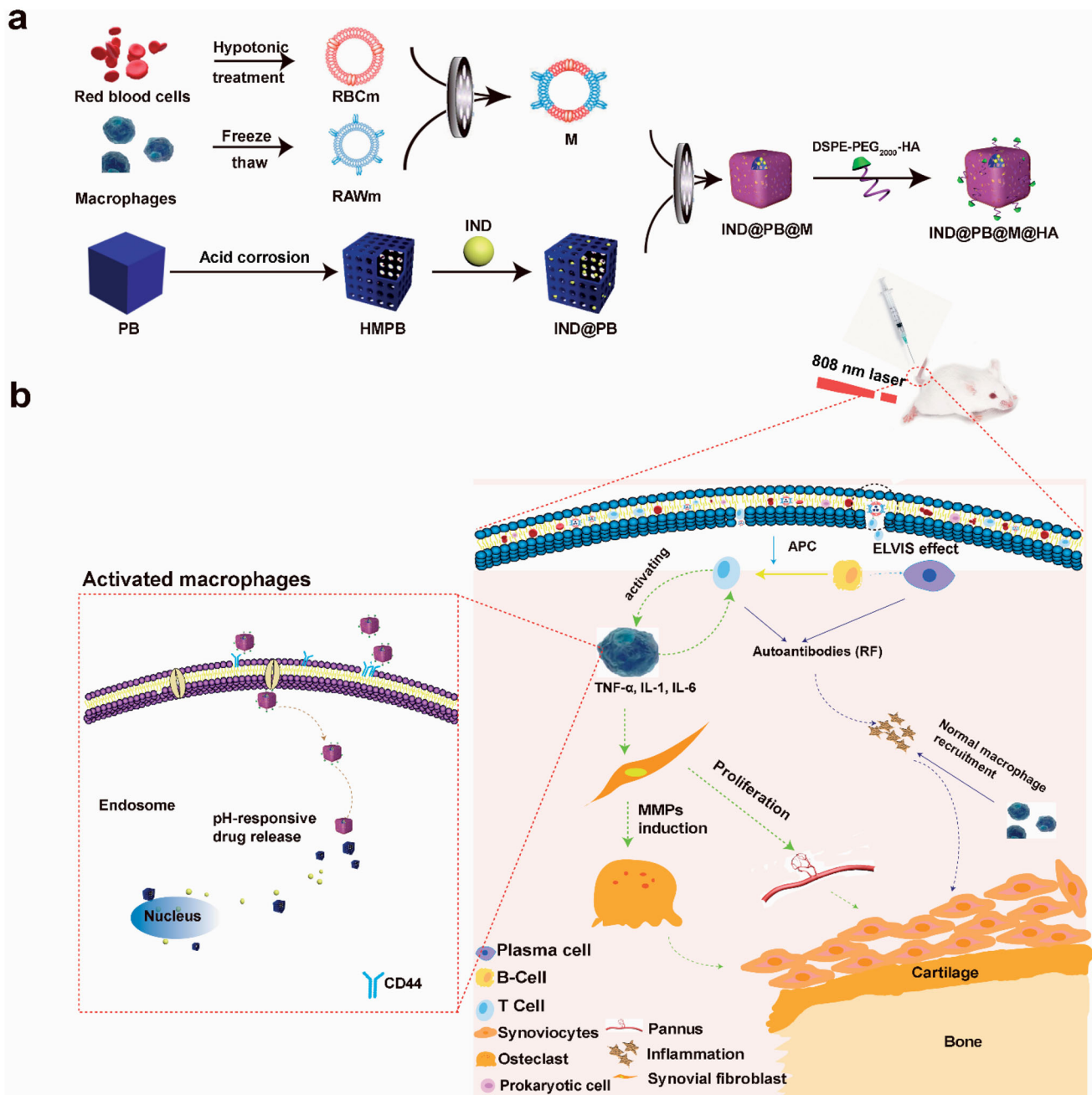
Figure 1. Schematic showing the synthesis process of IND@PB@M@HA NPs for efficient rheumatoid arthritis therapy. (a) Preparation scheme of the nanosystem (IND@PB@M@HA NPs). (b) Proposed mechanism for IND@PB@M@HA NPs-mediated anti-arthritis efficacy in the arthritic internal environment. RBCm: red blood cell membrane; RAWm: macrophage membrane; M: hybrid membrane; PB: Prussian blue NPs; HMPB: hollow mesoporous Prussian blue NPs; APC: antigen presenting cells.

demonstrated excellent pharmacodynamics of IND@PB@M@HA NPs in vitro and in vivo even at ultra-low doses of IND.

Materials and methods

Cell lines and animals

Human fibroblast-like synovial cell line (HFLS), human RA fibroblast-like synovial cell line (RA-FLS), mouse macrophage cell line (RAW264.7 cells), human umbilical vein endothelial cells (HUVEC), human smooth muscle cells (SMC), human normal liver cells (HL7702), and cardiomyocyte cell (H9C2) were purchased at the Cell Bank of the Chinese Academy of Sciences (CAS) (Beijing, China) that with certification of authentication and free from Mycoplasma. Cells were cultured in Dulbecco's modified Eagle's medium (DMEM) (HyClone, Shanghai, China) supplemented with 10% fetal bovine serum (FBS) (Gibco, Shanghai, China) and 1% active ingredient and strepto-mycin (Invitrogen, Shanghai, China) at 37 °C and 5% CO (Thermo Scientific 8000 Incubator, Langenselbold, Germany).

Male Sprague-Dawley (SD) rats (No. 11001121102351972) were purchased at the Beijing Vital River Laboratory Animal Technology Co. and fed in the Laboratory Animal Centre of Hunan University of Chinese Medicine (HNUCM) (License no. SYXK[Hunan]2019-0009). Water and food were provided during the experiments. Animal care and experimental procedures were approved by the Institutional Animal Care and Use Committee of HNUCM and conducted in strict accordance with the National Institutes of Health (NIH) Guidelines for the Care and Use of Laboratory Animals (Bethesda, MD, USA).

Preparation of RBC-RAW-hybrid membranes (M) and membranes fusion study

Red blood cell membranes (RBCm) and macrophage membranes (RAWm) were prepared based on our previous report with some modifications [22]. A BCA protein assay kit (Solarbio Life Sciences, Beijing, China) was employed to quantify the protein concentration of RBCm and RAWm (see methods in Supporting Information).

Preparation of RBC-RAW-hybrid membrane (M)

RBC-RAW-hybrid membranes (M) were prepared as described previously [23]. In brief, red blood cell membranes (RBCm) and macrophage membranes (RAWm) were mixed with the same membrane protein weight ratio and then stirred at 37 °C for 2 h after sonication (50 W, 5 min) to avoid spontaneous fusion into nanoscale vesicles until extruded through 200 nm porous membranes (HandExtruder, Suzhou, China).

Membrane fusion study

Förster resonance energy transfer (FRET) assay was used to observe the membrane fusion process [24]. The DiI (lex/lem = 549/565 nm) and DiD (lex/lem = 644/663 nm) was employed to label the RAWm. Then, the RBCm, was increasingly added into the dyes-doped RAWm for fusion (the weight ratios of 0:1, 1:1, 3:1 and 5:1, respectively). The fluorescence spectra were recorded at an excitation wavelength of 525 nm and an excitation wavelength of 550–750 nm emission spectrum. Thereafter, the fusion assay of different membranes was performed based on previous studies [23]. In brief, RBCm and RAWm were stained with DiI (red fluorescence) and DiO (green fluorescence), respectively. After membranes were stirred for 30 min in the dark, the separate membrane solutions were mixed, followed by ultrasonic treatment

for 3 min and stirring for 2 h to complete the membrane fusion process. Finally, the RBC-RAW-hybrid membrane vesicles were collected by centrifugation (12,000 rpm, 30 min, 4 °C) and re-suspended in the water for fluorescence image under the CLSM (Olympus FV1200, Tokyo, Japan).

Preparation and characterisation of IND loaded in PB nanoparticles

The PB NPs were synthesised according to our previous report and shown in the Supporting Information [22]. The IND-loaded PB NPs (IND@PB NPs) were synthesised by mixing various concentrations of IND (3, 4, 5, 6 mg/ml, 500 μl) with PB NPs (1 mg/ml, 500 μl). The mixture was stirred at 25 °C for 16 h and then centrifuged at 12,000 rpm for 30 min to collect the IND@PB NPs. The surface zeta potentials and size distribution of the nanomaterials were measured using a Zetasizer Nano analyser (Malvern Nano Series, Malvern, UK). The optical characteristics of different NPs were characterised by the UV-Vis spectrophotometer (DU800, Beckman Coulter, California, USA), FTIR, X-ray photoelectron spectroscopy (XPS), and X-ray diffraction (XRD) (Puchuan Testing Co., Guangdong, China).

To determine the content of IND@PB NPs, the obtained supernatant of unencapsulated IND after centrifugation was subjected to the UV-Vis measurement. The concentration of unloaded IND was determined according to the standard calibration curve. The loading efficiency (LC) and encapsulation efficiency (EC) of IND were calculated based on the following equations:

$$LC\ (\%)\ =\ IND\ weight\ in\ NPs/total\ NPs\ weight\ \times\ 100\%$$
$$EC\ (\%)\ =\ IND\ weight\ in\ NPs/total\ IND\ weight\ \times\ 100\%$$

Preparation of hyaluronic acid grafting polyethylene glycol (HA-PEG$_{2000}$-DSPE)

The hyaluronic acid grafted polyethylene glycol (HA-PEG$_{2000}$-DSPE) was prepared as described previously [22]. 5 mg of HA (Dalian Meilun Biotechnology, Dalian, China), 50 mg of NHS, and 25 mg of EDC (Ponsure Biotech Nology, Shanghai, China) were dissolved in 1 ml of PBS and then mixed stirring at room temperature for 30 min. Then, 25 mg of DSPE-PEG$_{2000}$-NH$_2$ (Sigma-Aldrich, Shanghai, China) was added into the solution and mixed stirring for 24 h. And the resulting solution was dialysed by a dialysis bag (MWCO of 2.5 kDa) in deionised water and following lyophilised and stored at 4 °C for future applications.

Preparation and characterisation of IND@PB@M@HA NPs

The IND@PB NPs (5 mg/ml, 100 μl) were mixed with 400 μl of hybrid membranes (2.5 mg/ml). The mixture was stirred at 37 °C for 2 h after sonication (50 W, 5 min). Finally, the solution was extruded through a 200 nm porous membrane and the uncoated membrane was removed through centrifugation and washed until no protein was in the supernatant to obtain the IND@PB@M NPs.

Thereafter, 0.1 ml of HA-PEG$_{2000}$-DSPE in PBS (5.0 mg/ml) was added into 1 ml of the IND@PB@M NPs solution (1 mg/ml PB), mixed thoroughly, and stirred for 1 h at 37 °C. Finally, HA-PEG$_{2000}$-DSPE was inserted into the membrane and obtained IND@PB@M@HA NPs after removing free HA-PEG$_{2000}$-DSPE by centrifugation. The surface zeta potential and size distribution of the nanomaterials were measured using a Zetasizer Nano analyser. The morphology of the dry NPs was analysed using transmission electron microscopy (TEM, JEOL JEM1400plus, Tokyo, Japan).

In vitro *pH-triggered drug release*

To monitor the *in vitro* release behaviour of IND. First, IND@PB@M@HA NPs were dissolved in the pH 7.4 and pH 5.4 PBS containing 0.5% (v/v) Tween 80, respectively, with final concentration of 5 mg/ml. Then, the centrifuge tubes containing 5 ml solution were shaken constantly and gently at 37 °C. During the release process, 1 ml of the release solution after centrifugation of the original solution (12000 rpm, 10 min) was taken out at different time points (1, 2, 4, 6, 8, 12, 24, 48, and 72 h), and the equivalent fresh buffers with different pH values were added back to the tube to keep volume stability. The amount of cumulative IND release was measured by a UV-Vis spectrophotometer according to the calibration curve. All experiments were repeated three times.

In vitro *photothermal properties and stability*

Samples of PB, IND@PB, IND@PB@M, and IND@PB@M@HA solutions (with PB concentration of 0.1 mg/ml) and PBS were irradiated with an 808 nm laser (1 W/cm^2, 5 min). The temperatures were recorded every 1 min using a thermal infrared imaging camera (Flir C2, Shanghai, China). Active ingredient green (ICG, Thermo Scientific, Shanghai, China) was used to compare the photothermal stability with PB-based nanomaterials, and the cycle in which the solution of IND@PB@M@HA and ICG (0.1 mg/ml) was irradiated by an 808 nm laser (1 W/cm^2, 5 min) and then cooled down to room tem-perature was repeated several times. Thereafter, the changes in ingredients of ICG and IND@PB@M@HA before and after laser irradi-ation were detected by a UV-Vis spectrophotometer.

Immune evasion assay

After RAW264.7 cells were cultured in 12 well plate for 24 h, Rho@PB and Rho@PB@M@HA (see methods in Supplementary Information for synthesis) were added into the cells and incubated for 4 h. Cell nuclei were stained by Hoechst33342 (Yeasen Biotechnology, Shanghai, China) and images were collected by the CLSM.

In vitro *targeting assay*

To investigate the uptake ability of cell membrane-modified NPs into cells, the HFLS, RA-FLS, normal, and lipopolysaccharide (LPS)-induced RAW264.7 cells were cultured in 12 well plates for 24 h. Thereafter, cells were incubated in fresh media containing Rho@RBCm, Rho@RAWm and Rho@M NPs (PB 30 μg/ml) for 4 h. Cell nuclei were stained with Hoechst33342 before being imaged using the CLSM.

To investigate the uptake ability of IND@PB@M@HA NPs into cells, the RAW264.7 cells were inoculated into 12-well plates (5 × 10^4 cells) and cultured for 24 h with or without 100 ng/ml of LPS (Sigma-Aldrich, Shanghai, China). To further explore the targeting capacity of HA-modified nanoparticles, cells were pretreated with 500 μg/ml of free HA for 1 h, and then incubated with fresh media containing Rho@PB@M or Rho@PB@M@HA NPs for 4 h. Cell nuclei were stained with Hoechst33342 before being imaged using the CLSM.

In vivo *biodistribution and pharmacokinetics study*

Targeting and bio-distribution assay of ankle joints

ICG, ICG@PB, ICG@PB@M and ICG@PB@M@HA NPs (see Methods in Supplementary Information for synthesis) were injected intravenously into adjuvant-induced arthritis (AIA) rats with an equivalent ICG concentration (5 mg/kg). Thereafter, at 0, 4, 8, 12, 24, and 36 h after management, the ICG fluorescent signals were collected using the IVIS dynamic optics system. AIA rats were then sacrificed to collect the major organs and ankle joints. Fluorescence images were captured, and the intensities of these organs or ankle joints were obtained using an IVIS dynamic optics system (PerkinElmer, Massachusetts, USA).

Pharmacokinetics assay

The AIA rats were injected with ICG, ICG@PB and ICG@PB@M@HA NPs (ICG, 5 mg/kg) *via* the tail vein once. Subsequently, 200 μl blood samples were drawn from the jugular vein at planned time points (1, 2, 4, 6, 8, 12, 24 and 48 h) and centrifuged (3000 rpm, 4 °C) for 10 min and analysed using an IVIS dynamic optics system.

Analysis of biocompatibility

Haemolysis assay: RBCs were collected and separated through centrifugation (3000 rpm, 5 min) from the blood of SD rats. The RBC suspension (4% in PBS, v/v) was incubated with various concentrations of IND, PB, IND@PB, IND@PB@M, and IND@PB@M@HA NPs (0, 25, 50, 100 and 200 μg/ml PB) at 37 °C for 4 h. After centrifugation (3500 rpm, 4 °C) for 5 min, the supernatant was collected, and the absorbance was measured at 562 nm. The solutions of RBCs were mixed with pure water as a positive control and with PBS as a negative control, respectively. The haemolysis rate was calculated based on the following equation:

$$\text{Haemolysis }(\%) = (OD_{sample} - OD_{PBS}/OD_{water}) \times 100\%.$$

Thrombo-test: Platelet-rich plasma was extracted from the whole blood of adult healthy SD rats for coagulation assay. In brief, platelet-rich plasma was incubated with 1× PBS, thrombin (1%, v/v), PB, IND@PB, IND@PB@M, and IND@PB@M@HA NPs (100 μg/ml) and incubated for 6 h at 37 °C. Absorbance was measured by the microplate reader at 650 nm. Blood samples treated with PBS and thrombin were used as negative and positive controls, respectively. The turbidity rate was calculated as follows:

$$\text{Turbidity }(\%) = (OD_{sample}/OD_{PBS}) \times 100\%.$$

Cell viability

The efficacy of IND, PB, IND@PB and IND@PB@M@HA NPs was evaluated in RA-FLS and LPS-induced RAW264.7 cells, and toxicity evaluation was conducted on HFLS, HUVEC, SMC, HL7702 and H9C2 cells. After seeding the cells in a 96-well plate for 24 h, the culture solution was removed and replaced with a fresh medium containing different concentrations of IND, PB, IND@PB, and IND@PB@M@HA NPs. After RA-FLS and LPS-induced RAW264.7 cells were cultured for 48 h, and HFLS, HUVEC, SMC, HL7702 and H9C2 cells for 24 h, respectively, 100 μl of MTT (Sigma-Aldrich, Shanghai, China) solution was added to each well and incubated for 4 h. Thereafter, the supernatant was removed carefully and the crystal violet was dissolved with 100 μl of DMSO. Finally, the absorbance was measured at 490 nm using a microplate reader (EnSpire 2300, PerkinElmer, Massachusetts, USA) (Cell Viability = (OD $_{sample}$-OD $_{back\ ground}$)/(OD $_{control}$-OD $_{back\ ground}$) × 100%).

Safety comparison with Ag NPs

The preparation of Ag NPs referred to the synthesis method of predecessors [25]. Briefly, 3.8 mg sodium borohydride and 8.82 mg trisodium citrate were added into 9 ml deionised water and stirred

at 4 °C for 30 min, then 1 ml AgNO$_3$ (10 mM) was added, followed by a reaction for 30 min. Finally, a generated golden yellow Ag NPs solution was generated and stored at 4 °C for further use.

The toxicity evaluation of Ag and PB NPs was conducted on the HUVECs. After seeding the cells into a 96-well plate, different concentrations of PB and Ag NPs were added. After culturing for another 24 h, the viability assay of cells was performed using the MTT test.

Enzyme-linked immunosorbent assay (ELISA) assay

When the density of RAW264.6 cells in the 24-well plate reached about 60%, different components of the IND, PB, IND@PB, IND@PB@M or IND@PB@M@HA NPs were added. After 2 h, LPS (final concentration of 100 ng/ml) was added and the cells were cultured for 24 h. The contents of supernatant tumour necrosis factor-alpha (TNF-α) and interleukin-6 (IL-6) were detected using ELISA kits for TNF-α and IL-6 (Neobioscience, Shenzhen, China, #EMC102a and #EMC004 respectively), and the lower layer of cells was photographed under an inverted fluorescence microscope.

Detection of cellular ROS

The LPS-induced RAW264.7cells and normal cells were seeded in a 12-well plate and incubated for 24 h at 37 °C and 5% CO$_2$. The components including PBS, IND (8 μg/ml), PB, IND@PB@M and IND@PB@M@HA NPs (equivalent PB concentration: 40 μg/ml) were added into the cells and incubated for 4 h. DCFH-DA (Yeasen, Biotechnology, Shanghai, China) probe was then added to the cells in each well and incubated for 30 min followed by imaging under an inverted fluorescence microscope.

Therapeutic efficacy in vivo

A commonly-used experimental model of RA, adjuvant-induced arthritis (AIA), was established according to a previously described method [26]. In brief, specific-pathogen-free (SPF) male SD rats aged 4–5 weeks were injected subcutaneously into the base of the tail with 0.1 ml of complete Freund's adjuvant (CFA) containing 300 μg of ground heat-killed Mycobacterium tuberculosis H37Ra (Mtb) (BD Difco 8138819, USA) suspended in mineral oil (M8410, Sigma-Aldrich, Shanghai, China).

AIA rats were randomly assigned into five groups (n = 6) for and administered with saline, IND (0.1 mg/kg, BW), PB@M@HA NPs (equivalent PB concentration: 1 mg/kg, BW), IND@PB@M@HA NPs and IND@PB@M@HA NPs with laser irradiation (equivalent PB concentration: 1 mg/kg, BW). All groups were injected intravenously from the beginning of modelling with different formulations every two days for a total of 18 times. Normal control rats without any intervening measures were served as negative controls. The hind paw volume, joint pain-related score and body weight were measured every three days. The joint pain-related scores range from 0 to 4, with a maximum score of 16 [27]. On days 2, 12, 21, and 30, the rats were photographed to observe the swelling of the feet. At the end of the study, the rats of blood sample, ankle joints, heart, liver, spleen, lung, and kidney were collected. Whole blood samples were centrifuged at 3000 rpm at 4 °C for 10 min to collect the serum from the supernatant. Subsequently, serum samples were immediately frozen at −80 °C until analysis using the Bio-Plex Pro Assays kit (Bio-Rad, California, USA) to quantify cytokines. The tissue and part of the ankle joint sections were stained with haematoxylin and eosin (H&E) to evaluate the histological changes

with synovial hyperplasia and ankle cartilage erosion. The sections were imaged using an inverted fluorescence microscope. Another part of the ankle joint was subjected to Micro-CT imaging (PerkinElmer-Caliper LS Quantum FX Demo, Massachusetts, USA) to observe the bone erosion situation.

Safety evaluation

At the end of the experiments, blood samples were collected from rats for biochemical and hematological assays. Major organs including the heart, liver, spleen, lungs, and kidneys were harvested for frozen slices and H&E staining.

Statistical analysis

All quantitative parameters were presented as the means ± SEM. All data were analysed using the Student's two-sided t-test or two-way analysis of variance (ANOVA). A significant difference was considered when the P-value was less than .05.

Results and discussion

Characterisation of NPs

The physiochemical properties of IND@PB@M@HA NPs were characterised using different methods. TEM images in Figure 2a exhibited the hollow mesoporous PB NPs with a uniform size of approximately 120 nm. However, IND@PB@M@HA NPs demonstrated a characteristic core-shell structure [23] with a uniform outer membrane shell (Figure 2b), the result of which is consistent with our previous report [22]. Figure 2c showed the relative encapsulation efficiency of PB NPs at different weight ratios of PB/IND. In the context of release and encapsulation efficiency, an optimal ratio of 1:5 was chosen for the compound of IND@PB@M@HA NPs. Next, the impact of membrane coating and HA modification on the particle size and surface zeta potentials of IND@PB@M@HA NPs were measured. Figure 2d indicated that the surface zeta potential of IND@PB@M@HA NPs varied from ∼−11.57 mV of IND@PB NPs to ∼−8.66 mV. The particle size gradually increased with the encapsulation of the hybrid membranes and HA (Figure 2e). In addition, the UV-Vis spectrum showed the peaks of PB NPs at 725 nm, RBCm at 405 nm, and IND at 320 nm and 266 nm, respectively. The FT-IR spectra showed a characteristic absorption peak of PB NPs at 2080 cm^{-1}, and IND at 3450 cm^{-1}. The XPS spectra investigated the chemical composition of nanomaterials, such as Fe2p3 of PB NPs and Cl2p of IND (Figure S1). Beyond that, the good dispersion of IND@PB NPs demonstrated the high solubility of IND in the water after being encapsulated by the PB carrier (Figure S2).

As chronically inflamed joints showed a weakly acidic microenvironment (pH 5.0–6.0) due to the increased metabolic rate of inflamed synovium and poor perfusion of oxygen [21,28], which can be used to control drug release through hypoxia and pH-sensitive manners after nanoparticles are located in the inflammatory tissue. By investigating the effect of pH value on the drug release behaviour of IND@PB@M@HA NPs in vitro, IND@PB@M@HA NPs showed 62.7% and 29.2% drug release at 24 h; 72.9% and 31.2% drug release at 48 h at pH 5.4 and pH 7.4 buffer, respectively (Figure 2f). This result confirmed an acid-dependent release manner of IND. We then explored the cellular distribution of IND@PB@M@HA NPs. Blue, green, and red fluorescence represented the signals of the nucleus, lysosome, and IND@PB@M@HA, respectively. CLSM images reflected by

the yellow fluorescence showed that some of IND@PB@M@HA NPs were located in lysosomes after entering into cells. As shown in Figure S3, the co-localization of lysosomes with IND@PB@M@HA NPs indicated that most of the NPs were mostly distributed in the lysosomes at 4 h. These results suggested that such an encapsulation system could fulfil the requirements of an on-demand delivery system of drugs into a slightly acidic intracellular microenvironment in the inflammatory tissue.

Furthermore, fluorescence imaging and FRET were used to characterise the fusion efficiency assay of the membranes modified with these two dyes. The increased FRET signals were observed after the introduction of the red cell membranes, suggesting that a break in the FRET pair due to the interspersing of the two membrane materials (Figure 2g). Fluorescence imaging of DiI-labelled RBCm and DiO-labelled RAWm demonstrated a visualised yellow fluorescent signal after membranes fusion, directly suggesting a high incorporation efficiency of natural cell membranes fusion (Figure 2h). In addition, SDS-PAGE and Western blotting analyses were performed to verify the expression of fusion proteins. Compared with the natural RBCm or RAWm, nearly all protein bands of IND@PB@M@HA and IND@PB@M NPs were preserved (Figure S4a). Furthermore, we carefully studied the specific protein markers (CD11b for RAWm uniquely [29] and CD47 for both RBCm and RAWm) of the hybrid membranes and IND@PB@M@HA NPs. The results verified that CD47 was expressed by both RBCm and RAWm. In contrast, CD11b was only expressed on the macrophage membranes (Figure S4b). The existence of
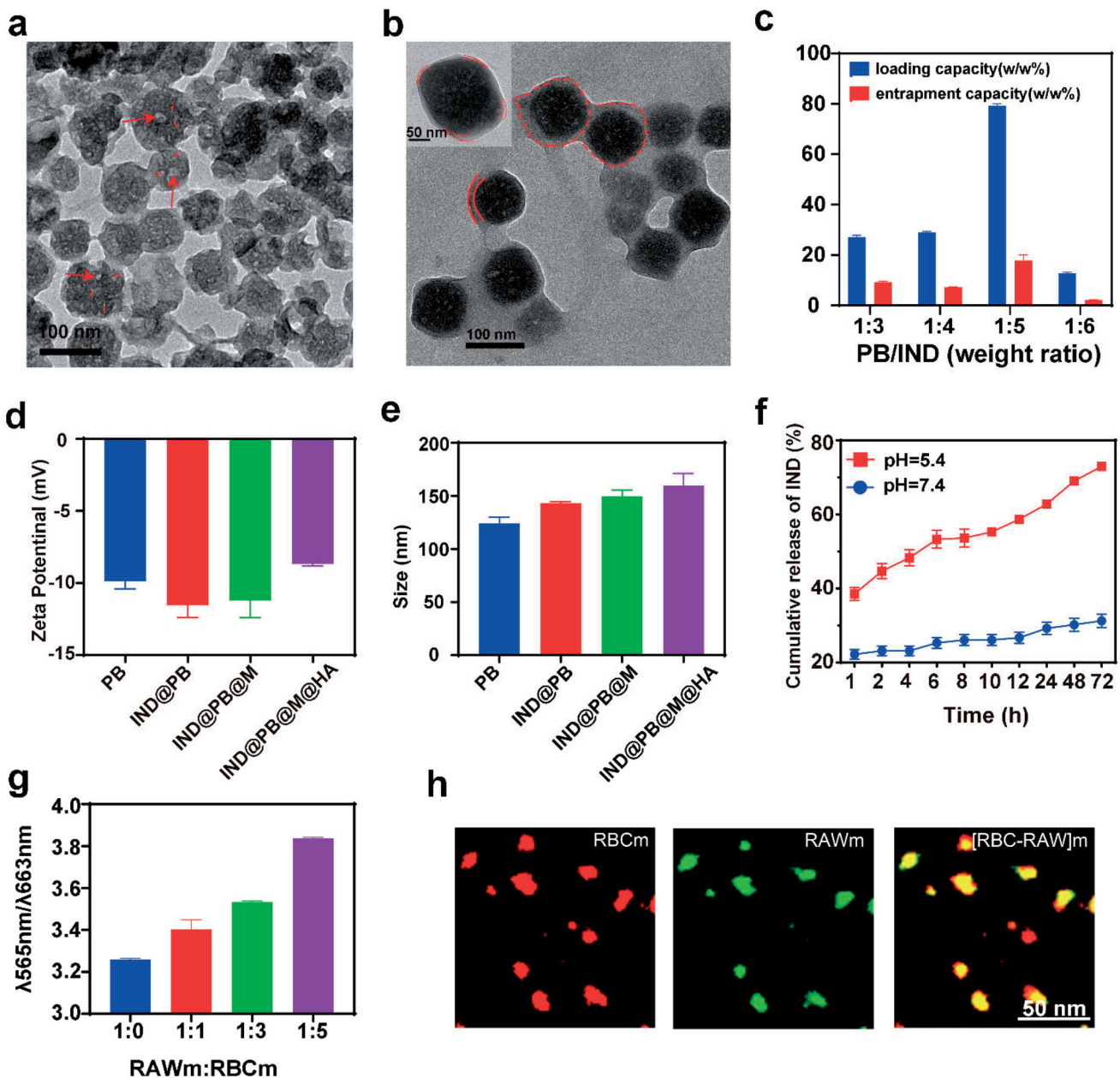

Figure 2. Characterisation of NPs and drug release behaviour in different buffer solutions: pH = 7.4 and pH = 5.4. TEM images of (a) hollow Prussian blue NPs and (b) IND@PB@M@HA NPs. (c) IND loading and encapsulation efficiency of PB NPs when the weight ratio of PB and IND were 1:3, 1:4, 1:5 and 1:6, respectively. (d) Surface zeta potentials and (e) particle size distribution of PB, IND@PB, IND@PB@M and IND@PB@M@HA NPs. (f) IND release from IND@PB@M@HA NPs at two pH values (pH 7.4 and pH 5.4) at 37 °C. (g) FRET investigation of membranes fusion. (h) Membrane fusion of two kinds of membranes imaged by the CLSM. RBCm were labelled with DiI (red), RAWm were labelled with DiO (green).

these markers endowed the enhanced immunity escaping ability of hybrid membranes [30].

Photothermal properties of PB and its anti-arthritis potential *in vitro*

Firstly, we investigated the photothermal effect with laser irradiation and stability of PB NPs. Meanwhile, ICG, a commonly used light sensitiser, was used as the control [31]. Figure 3a indicated that the maximal temperature of IND@PB@M@HA NPs did not change remarkably after laser irradiation. However, the highest temperature of ICG began to decline after laser irradiation at

75 min and was lower than that of IND@PB@M@HA NPs at 115 min. The temperature increase of IND@PB@M@HA after laser irradiation for 5 cycles was still maintained at about 18.7 °C, whereas that of ICG gradually decreased with the cycle increase of laser irradiation. Meanwhile, the UV-Vis absorption spectrum indicated the existence of a stable peak of IND@PB@M@HA NPs but not for ICG after 5 cycles of irradiation (Figure 3b). In addition, the constant temperature changes of IND@PB, IND@PB@M, and IND@PB@M@HA NPs confirmed the photothermal stability and high photothermal conversion efficiency of the PB NPs (Figure 3c). Moreover, AIA rats with IND@PB@M@HA NPs administration also observed a significant temperature increase for up to about 55 °C
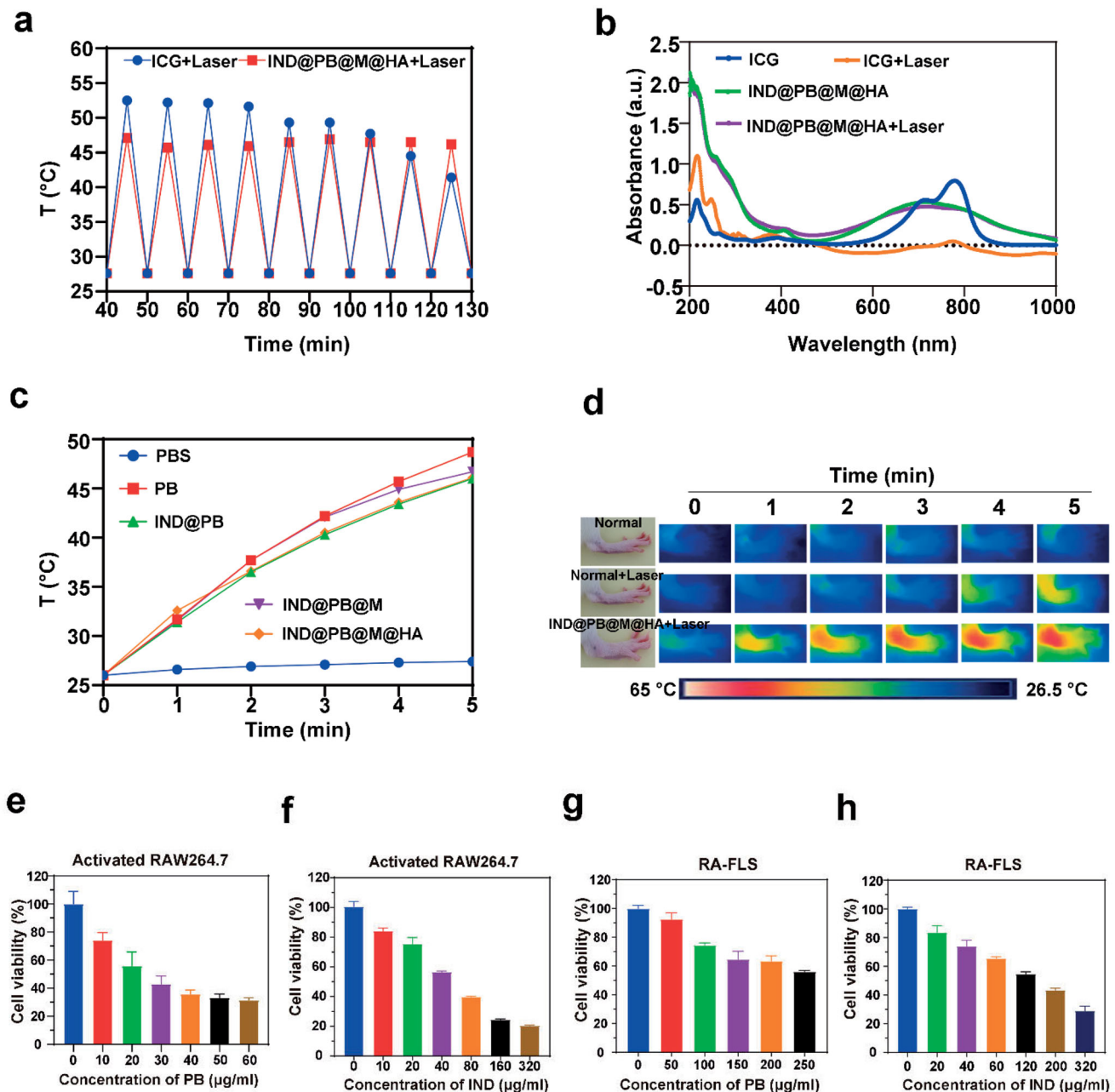

Figure 3. Photothermal properties of PB and its anti-arthritis potential *in vitro*. (a) Comparison of photothermal stability of IND@PB@M@HA NPs (0.1 mg/ml PB NPs) and ICG (0.1 mg/ml) under 808 nm laser irradiation (1 W/cm²). (b) The UV-Vis spectra of ICG (0.1 mg/ml) and IND@PB@M@HA NPs (0.1 mg/ml PB NPs) before and after 808 nm laser irradiation. (c) Temperature elevation curves of PBS, PB, IND@PB, IND@PB@M, and IND@PB@M@HA NPs (0.1 mg/ml PB NPs) during 808 nm laser irradiation (1 W/cm²) for 5 min. (d) IR thermal images of paws from AIA rats treated with 808 nm laser for 5 min (1 W/cm²). (e–f) The effect of free PB and IND concentration on LPS-treated RAW264.7 cells viability. (g–h) The effect of free PB and IND concentration on RA-FLS cells viability.

as the irradiation time extended. In control, the foot temperature of normal rats only slightly increased after with same treatment (Figure 3d).

In this study, we also found that both PB NPs and IND inhibit the viability of LPS-induced RAW264.7 and RA-FLS in a dose-dependent manner, which was consistent with the previous report [32,33]. MTT assay indicated that the half-maximal inhibitory concentration (IC_{50}) values of PB NPs and IND on LPS treated RAW264.7 cells were 20.81 μg/ml and 46.24 μg/ml, respectively (Figure 3e,f), which was significantly lower than that of RA-FLS (329.3 μg/ml and 113.5 μg/ml, respectively) (Figure 3g,h), Considering that RA-FLS mainly trigger the immune response and aggravate the disease for excessive proliferation, these results suggested that the combination of PB NPs and IND produced synergistic effect for therapy of RA mainly through collective anti-inflammation.

Biological function of hybrid membrane

As most of the nanomedicine can be cleared by the reticuloendothelial system during blood circulation, various biomimetic modifications were adopted to improve immune escape ability [14]. In this study, through incubating IND@PB@M@HA NPs with macrophages to mimic the immune environment, we found that a stronger red fluorescence signal was observed in PB NPs-treated cells, particularly at a high concentration (30 μg/ml) compared with that of the membrane-coated PB@M@HA NPs treated-cells (Figure 4a,b). This result clearly demonstrated that the membrane coating technology can enhance the immune escape ability of IND@PB@M@HA NPs. In addition, the enhancement of immune escape ability by membrane coating was reflected by the long circulation of half-life. Figure 4c indicated that the red blood cell membranes camouflage extended the blood retention time, and the half-life of ICG@PB@M@HA NPs ($\sim$3.09 h) in the AIA rats increased 2.78-fold compared to that of ICG@PB ($\sim$1.11 h). The result, which is comparable to the previous report [34], demonstrated that the biomimetic membrane coating can effectively prolong the blood circulation time by avoiding immune clearance.

As surface antigens of cell membranes were responsible for the homologous adhesion [23], we then investigated the targeting ability of PB@M to homotypic RA cells by observing the cellular uptake efficiency of inflammatory macrophages and RA-FLS, for rhodamine-labelled PB@M NPs. And normal RAW264.7 cells and
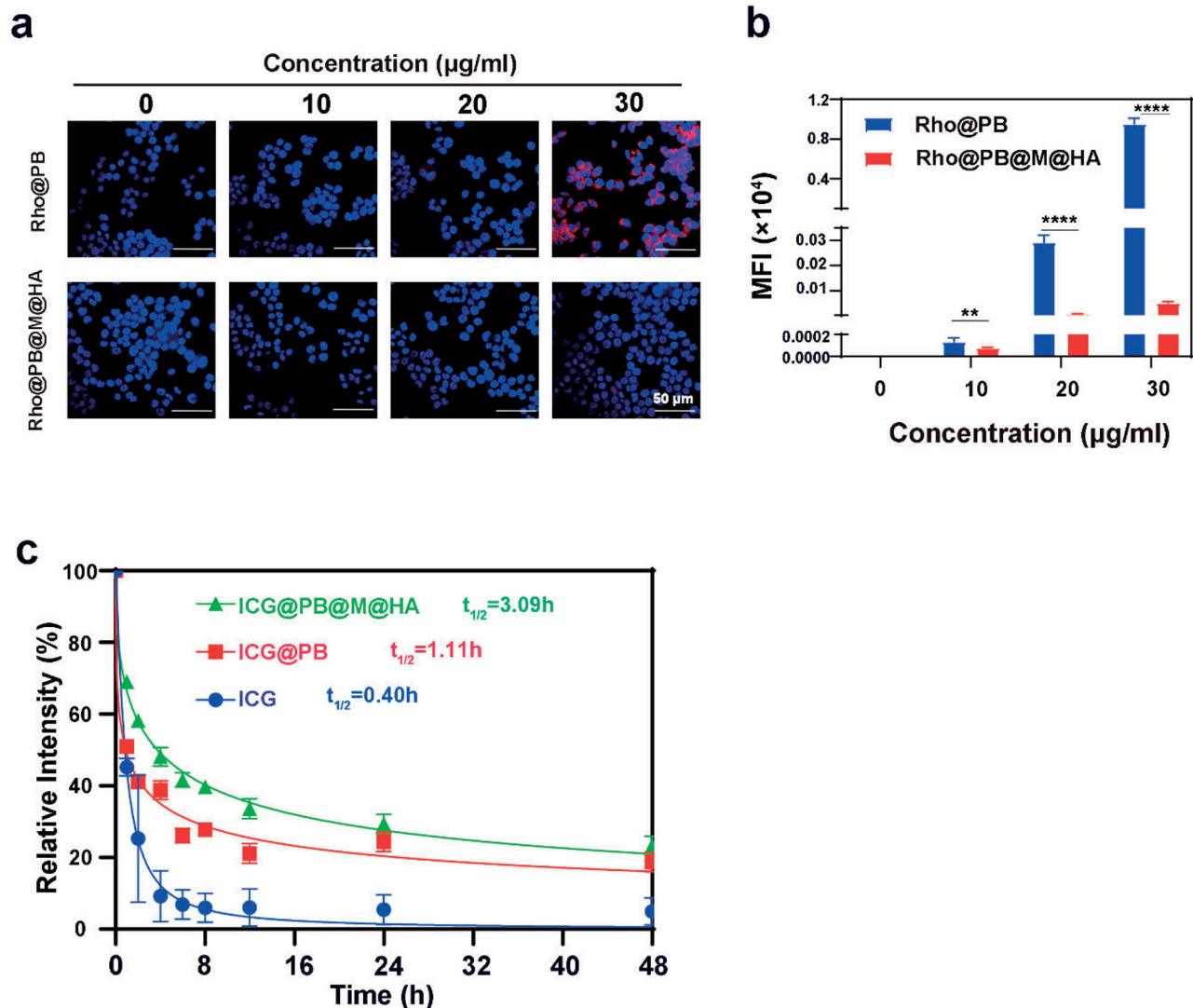

Figure 4. Membrane biological function characteristics assay. (a) Fluorescence images of the immune evading ability of hybrid membrane modified nanoparticles in RAW264.7 cells and (b) corresponding fluorescence signal quantitative analysis. Incubation time = 4 h. (c) Pharmacokinetic curves of ICG, ICG@PB, and ICG@PB@M@HA NPs after a single intravenous injection in AIA rats.

HFLS were used as the controls. As we expected that a stronger red fluorescence was observed in LPS treated RAW264.7 cells and RA-FLS than normal control groups after incubating with rhodamine-labelled PB@M NPs for 4 h (Figure S5). These results clearly indicated the targeting potential of the hybrid membranes owing to the homologous self-recognition capability of CD44 overexpression on the surface of macrophages and fibroblasts in inflamed joints of RA [20].

Targeting ability *in vitro* and *in vivo*

It has been reported that the interaction between ligand and specifically targeted receptor is an effective way to achieve nano-drug accumulation at target sites [35], we then investigated whether overexpressed CD44 receptor on the surface of activated macrophages can be used as a target to enhance the targeting ability of IND@PB@M@HA NPs to LPS-treated RAW264.7 cells. As we expected that the incubation of PB@M@HA NPs with LPS-induced RAW264.7 cells showed the strongest red fluorescence signal. In contrast, hyaluronic acid receptor blocking resulted in a significant decrease in the red fluorescence signal of PB@M@HA NPs in cells (Figure 5a,b). The above results confirmed that the specific interaction between HA and the CD44 receptor can effectively enhance the ability of drug delivery to inflammatory macrophages.

Next, we evaluated the targeting ability of ICG labelled IND@PB@M@HA NPs to the inflamed paw by monitoring the
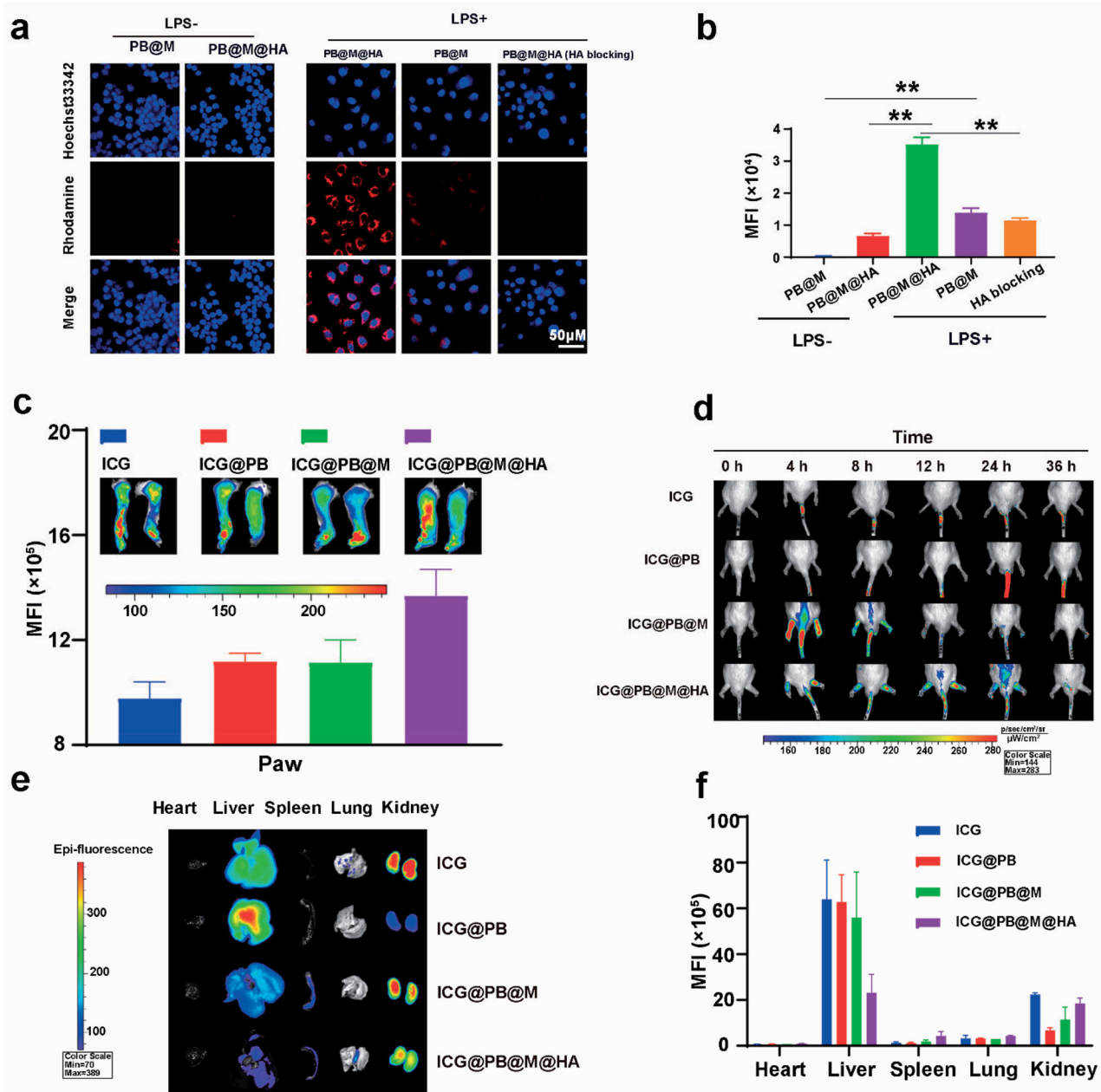

Figure 5. Targeting assay. (a) CLSM images of RAW264.7 cells after co-culture with PB@M NPs and PB@M@HA NPS or PB@M@HA NPs pre-treated with excessive HA and (b) corresponded fluorescence signal quantitative analysis. (c) Fluorescence quantitative and distribution analysis of paw after 36 h post-injection. (d) Biodistribution of ICG, ICG@PB, ICG@PB@M, and lCG@PB@M@HA NPs in AIA rats over time. Fluorescence distribution (e) and relative quantification (f) of heart, liver, spleen, lungs, kidneys.

fluorescence signal intensity in the paw at different time points. Compared with other groups, ICG@PB@M@HA NPs showed the strongest targeting capability (Figure 5c). Moreover, the high fluorescence intensity of ICG@PB@M@HA NPs in the paw can last up to 24 h. The long retention time of ICG@PB@M@HA NPs with a high concentration in the paws means that the drug can exert its efficacy at the highest utilisation rate. In contrast, the fluorescence intensity in the paw of mice with ICG@PB@M NPs administration reached a plateau at 4 h after drug injection, and the fluorescence signal began to decrease (Figure 5d). In addition, by monitoring the fluorescence distribution of major organs after 36 h post-injection, we found that a strong fluorescence signal was found in the liver and kidneys of all mice (Figure 5e,f). This result demonstrated

that the nanoparticles can be rapidly metabolised through the liver and kidneys. In addition, the fluorescence signal of the ICG@PB@M@HA NPs group increased in the spleen, which suggested the degradation of nanoparticles into ultra-small particles under acid conditions when they reached the swelling joint as particles smaller than 50 nm can distribute in the spleen [36].

Biocompatibility and safety assessment *in vitro*

To further verify the feasibility of IND@PB@M@HA NPs *in vivo*, we investigated their biocompatibility using different methods. Haemolysis assay images reflected directly the nontoxicity and good biocompatibility of PB-based nanoparticles (Figure 6a). In
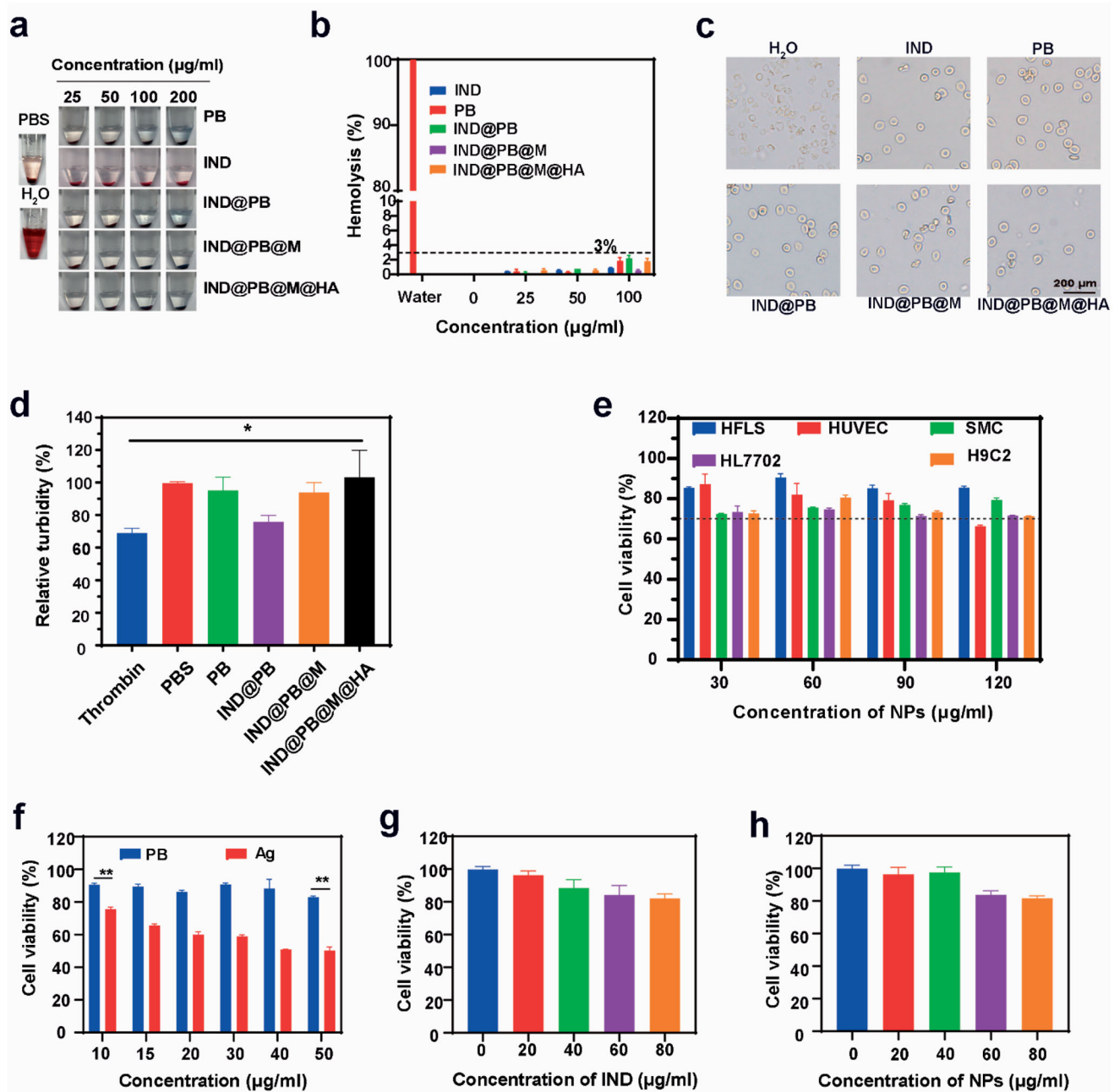

Figure 6. Biocompatibility assay. (a) Images of the haemolysis assay. Safety assessment of IND@PB@M@HA NPs. (b) Quantification of the haemolysis assay (concentration of IND is the amount contained in IND@PB NPs, other components equivalent concentration of PB NPs). (c) The microscopy images of red blood cells after co-culture with different materials for 4 h. (d) Platelet aggregation assay of PB, IND@PB, IND@PB@M and IND@PB@M@HA NPs (all components equivalent concentration of PB at 200 μg/ml). (e) The cell viability of HFLS, HUVEC, SMC, HL7702, and H9C2 cells after 24 h incubation with different concentrations of IND@PB@M@HA NPs. (f) Effects of Ag NPs and PB NPs on HUVEC cell viability. (g–h) Viabilities of RAW264.7 cells after incubation with various concentrations of IND and IND@PB@M@HA NPs.

addition, the haemolysis rates of all nanoparticles were less than 3%, even at a concentration of 100 μg/ml (Figure 6b). And our results showed the intact morphology of red blood cells in various nano-solutions at a concentration of 200 μg/ml (Figure 6c). Moreover, the coagulation test indicated the negligible risk of platelet aggregation following treatment with IND@PB@M@HA NPs, compared with the thrombin-positive group (Figure 6d). These results indicated the biocompatibility suitable for administration of IND@PB@M@HA NPs, which is promising for future *in vivo* applications.

MTT assay indicated the survival rates of various human normal cells (HFLS, HUVEC, SMC, HL7702 and H9C2) more than 70% after incubation with IND@PB@M@HA NPs at 120 μg/ml for 24 h, furthermore, NPs exerted anti-arthritic efficacy only at 40 μg/ml,

which demonstrated the acceptable cytotoxicity of IND@PB@M@HA NPs (Figure 6e). Yang *et al.* reported the efficiency of Ag NPs for RA therapy for the first time [37]; however, the MTT assay of HUVEC cells indicated that the toxicity of Ag NPs (50 μg/ml) was 5-fold greater than that of PB NPs at the same concentration (Figure 6f). This result clearly confirmed the clinical potential of PB NPs rather than Ag NPs for RA therapy.

In addition, we investigated the effect of nano-formulation on the toxicity of active ingredient. As shown in Figure 3f, the cell viabil-ity of inflammatory macrophages decreased 60% after co-incuba-tion with 80 μg/ml IND, however, the efficacy of which can be reached by IND@PB@M@HA (40 μg/ml, NPs) containing 6.4 μg/ml IND (Figure 7a). Meanwhile, we found that the viability of normal macrophages was only ~82% after co-incubating with 80 μg/ml
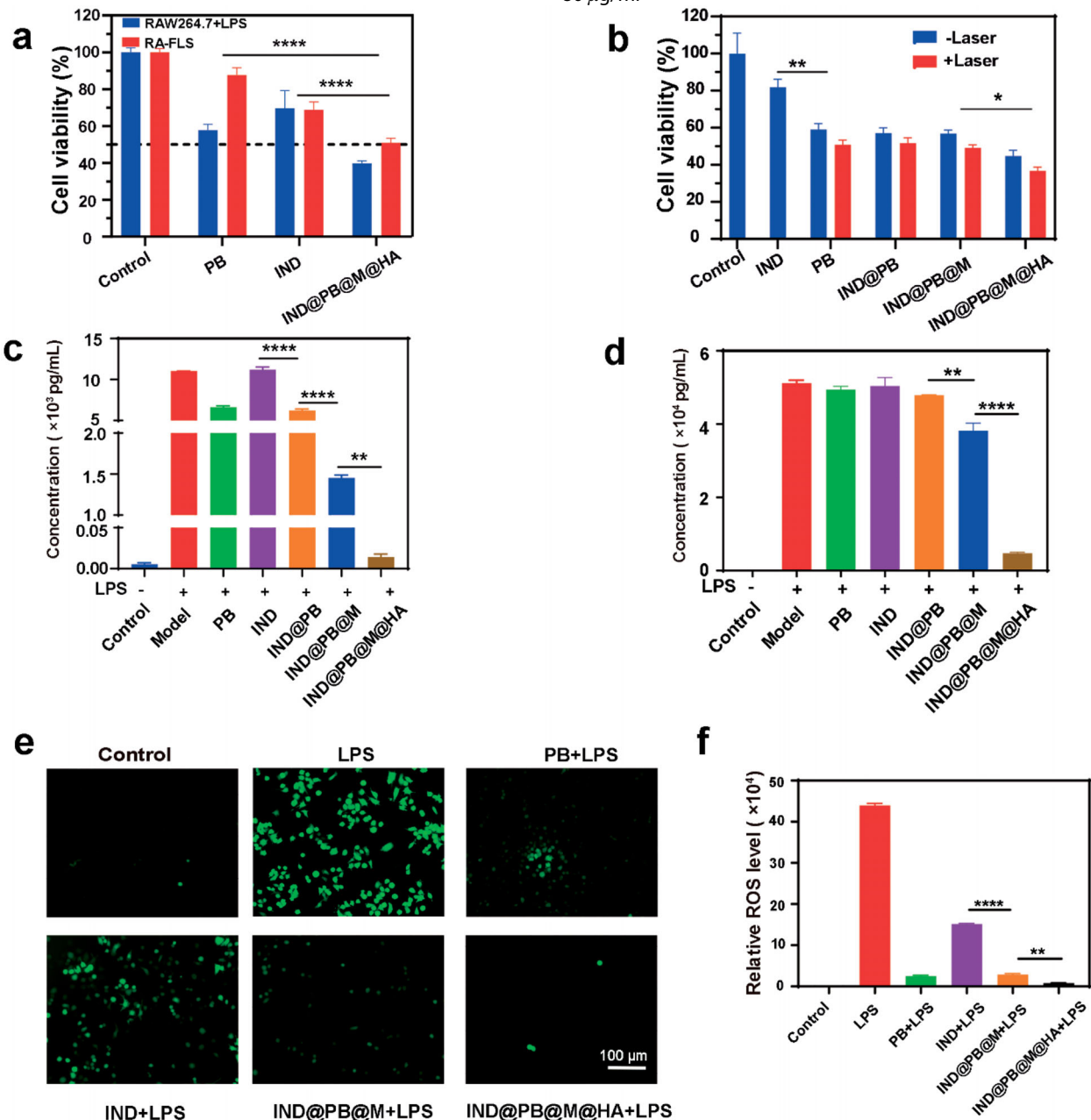

Figure 7. IND@PB@M@HA NPs decreased ROS production and the expression of pro-inflammatory cytokines of RAW264.7 cells stimulated by LPS. (a) The quantitative assay of cell viability after with different treatments. (b) The comparison quantitative assay of cell viability of activated macrophages with or without laser irradiation. Quantification of (c) IL-6 and (d) TNF-α in LPS induced RAW264.7 cells treated with different components of IND, PB, IND@PB, IND@PB@M, and IND@PB@M@HA NPs. (e) Inverted fluorescence microscope images of the relative ROS level of LPS induced RAW264.7 cells after co-culture with IND, PB, IND@PB, IND@PB@M, and IND@PB@M@HA NPs. (f) The corresponding statistical column histogram shows the relative ROS level.

IND (Figure 6g). In contrast, the negligible effect was found for IND@PB@M@HA (40 μg/ml, NPs) containing 6.4 μg/ml IND (Figure 6h). These results indicated that nano-formulation can significantly reduce the toxicity of IND.

The therapeutic effect of low-dose IND@PB@M@HA NPs on inflammation is greater than that of IND in vitro

Based on our goal for realising effective RA treatment with low toxicity, the pH-responsive IND@PB@M@HA NPs can realize on-demand drug release at the targeted sites of rheumatic joints.

Thus, the reduction of IND dosage did not affect the therapeutic efficiency. To verify this hypothesis, we performed a viability test of RA-FLS and inflammatory macrophage treated by free IND (40 μg/ml) and low-dose IND@PB@M@HA (containing 6.4 μg/ml of IND), and found that the cell viability of RA-FLS dropped from ~68.8% to ~50.9% and inflammatory RAW264.7 cells dropped from ~69.6% to ~39.8% after combinational treatment (Figure 7a). These results suggested that the combined application of PB NPs and IND can produce an augmenting effect for inhibiting the pathogenesis of RA. In addition, the cell viability of macrophages treated with LPS has further decreased by about 10% plus laser irradiation (Figure 7b).
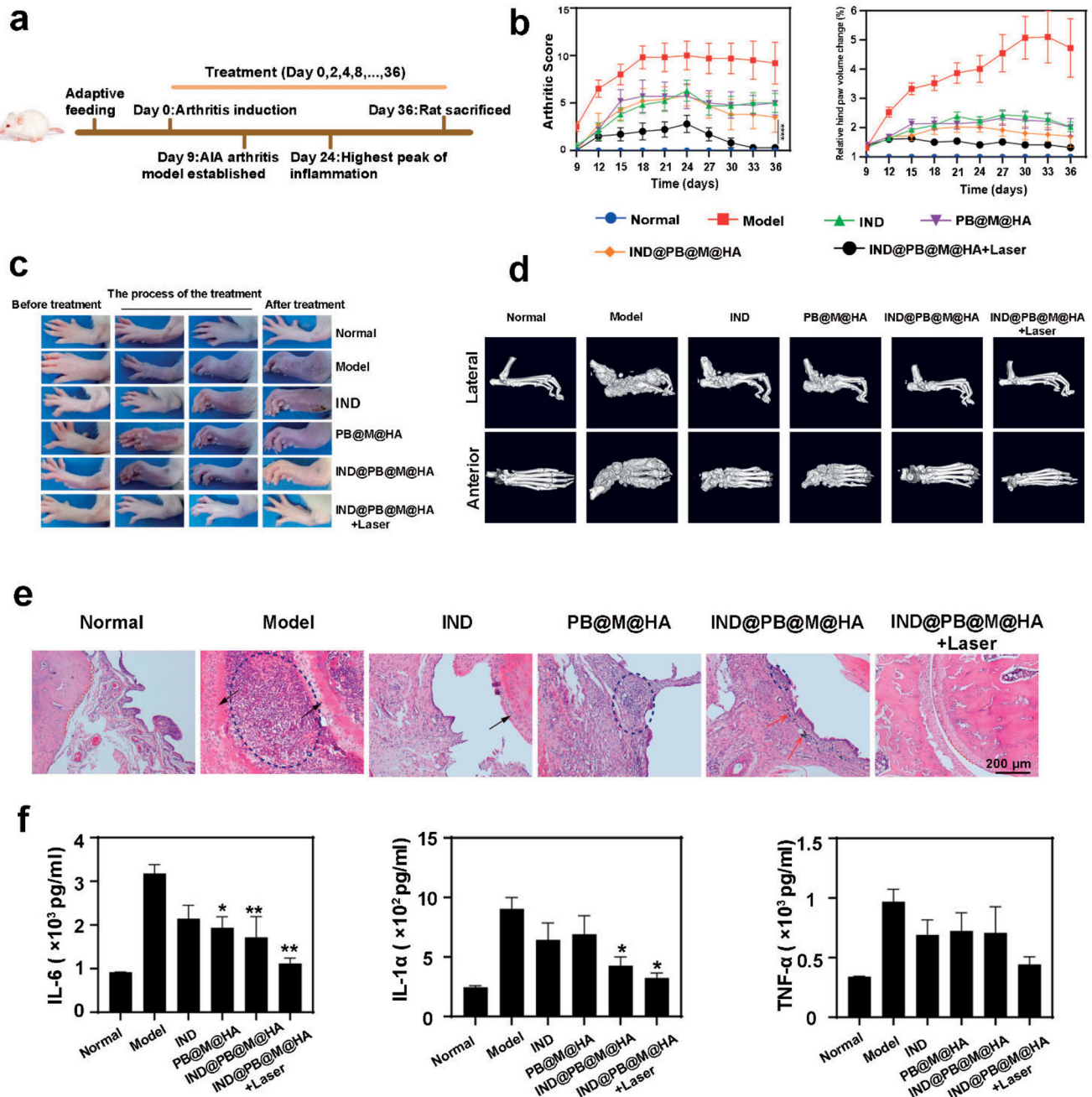

Figure 8. IND@PB@M@HA NPs containing low-dose IND reduce joint swelling and serum inflammation of AIA mice. (a) The schematic illustration of AIA rats' treatment. IND: 0.1 mg/kg, iv; PB@M@HA NPs: 1 mg/kg, iv; IND@PB@M@HA NPs: 1 mg/kg, iv. (b) Arthritic score and hind paw volume of AIA rats. * Indicating comparison with the model. (c) Photographs of the degree of ankle swelling during treatment. (d) Representative micro-CT images of ankle joints showing levels of bone erosion in ankle joints after different treatments. (e) H&E staining analysis of rat ankle joint after treatment. Black arrows indicate cartilage proliferation, red arrows indicate drug deposition in synovial tissue and circles indicate infiltration of inflammatory cells (original magnification $\times$ 100). (f) Expression of inflammatory factors. * Indicating comparison with the model.

During the progression of RA, ROS can act as both signalling molecules and mediators of inflammation to aggravate RA [38]. In addition, the release of ROS from activated inflammatory macrophages is another destructive factor in RA [39]. Based on the excellent catalytic properties of PBzyme for scavenging ROS and anti-inflammatory ability [40], we examined its efficacy against ROS and inflammatory factor levels in LPS treated macrophages. As shown in Figure 7c,d, compared with the model, IND@PB@M@HA NPs treatment significantly inhibited the levels of IL-6 and TNF-α ($\sim$11.02 ng/ml vs. $\sim$14.20 pg/ml; $\sim$51.15 ng/ml vs. $\sim$4.72 pg/ml, respectively). In addition, Figure 7e,f showed the strongest ROS-scavenging ability of IND@PB@M@HA compared with other materials. These results suggested that the IND@PB@M@HA NPs could significantly prevent LPS-induced intracellular ROS generation. Based on these results, we concluded that IND@PB@M@HA NPs can attenuate inflammation, which is more pronounced under photothermal therapy.

In vivo therapeutic effects on AIA rats

AIA rats were separately treated with IND (0.1 mg/kg), PB@M@HA (1 mg/kg of PB NPs), IND@PB@M@HA NPs and IND@PB@M@HA NPs with laser irradiation (1 mg/kg of PB NPs containing 0.1 mg/kg of IND) every other day, starting on modelling day and continuing for 36 days to investigate their therapeutic efficacy (Figure 8a). The normal and model groups were used as the negative and positive control, respectively. The arthritic score and relative hind paw volume change (the onset of severe
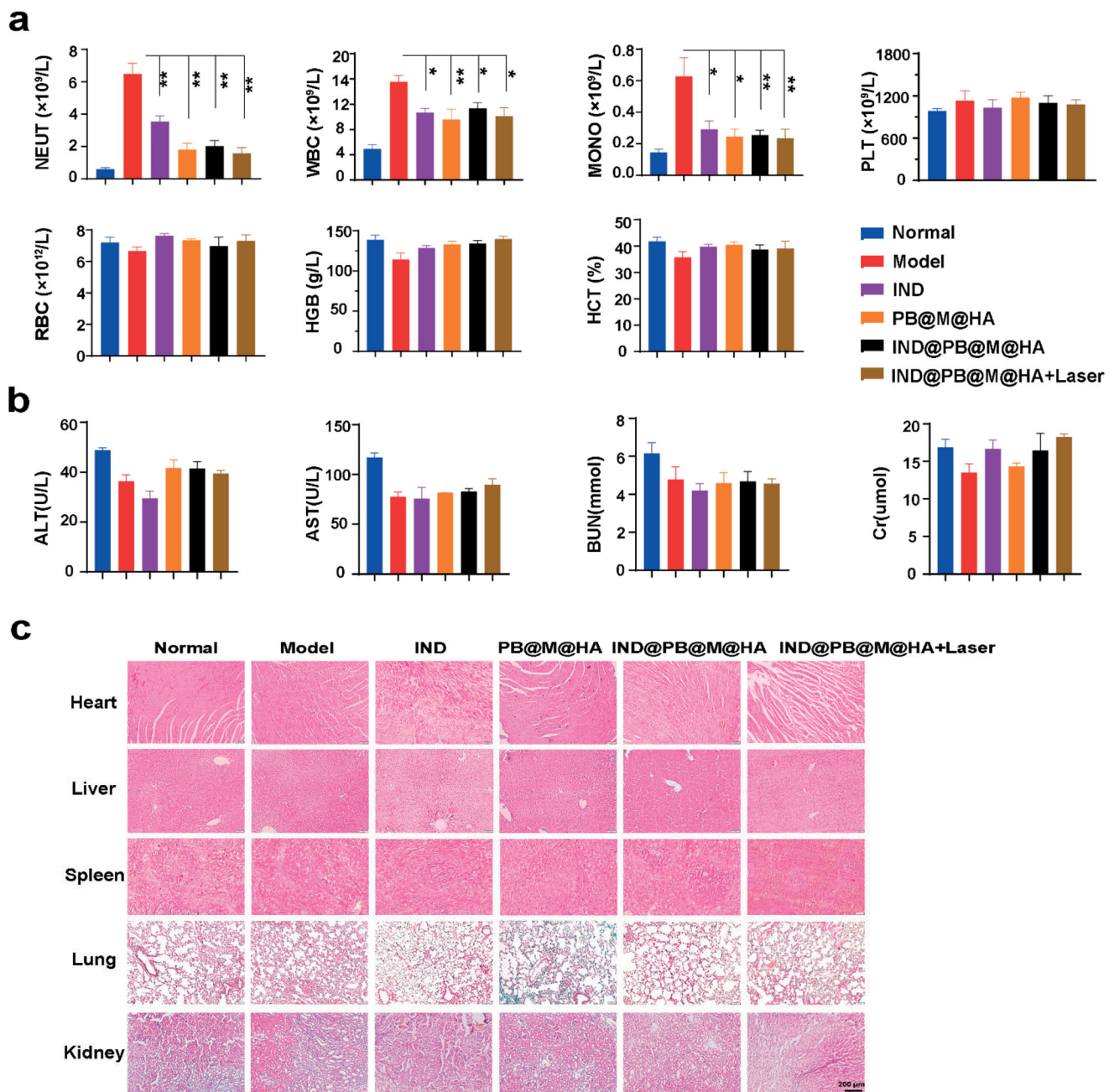

Figure 9. Toxicity evaluation in vivo: (a) Hematological analysis. (b) Hemato-biochemical analysis. (c) H&E staining of frozen slices of major organs. NEUT: neutrophil count; WBC: white blood cells; MONO: monocyte count; PLT: platelets; RBC: red blood cells; HGB: haemoglobin; HCT: haematocrit; ALT: alanine transaminase; AST: aspartate transaminase; BUN: blood urea nitrogen; Cr: creatinine.

arthritis) of AIA rats indicated the successful establishment of the RA model (Figure 8b). Compared with the model group, all drug interventions exhibited obvious amelioration in the degree of redness and swelling of rats. Among them, IND@PB@M@HA NPs plus photothermal therapy showed the strongest therapeutic effect, which was reflected by the disappearance of redness, swelling, and bone erosion suppression. However, the IND and PB@M@HA NPs treatment groups inhibited the disease progression only in some extent during the administration (Figure 8c). Micro-CT was further used to evaluate the effect of IND@PB@M@HA NPs and found the administration can block bone erosion and cartilage disruption (Figure 8d). The calcareous of the model group showed severe bone damage and grievous bone erosion extending to the metatarsals. However, compared with the model group, the bone erosion of ankle joints was differentially reduced after drugs treatment. Moreover, the therapeutic effect of IND@PB@M@HA NPs outperformed that of the other groups. Interestingly, bone erosion was nearly disappeared in the ankle joint of rats with IND@PB@M@HA NPs plus laser irradiation treatment. H&E staining of ankle joint slices indicated the smooth cartilage surface in the control group without synovial hyperplasia. In the model group, the synovial tissues possessed hyperplasia and enormous inflammatory cell infiltration, which filled the entire articular cavity and caused cartilage erosion and articular cavity closure. The IND group and PB@M@HA NPs groups differentially alleviated these symptoms. In contrast, the IND@PB@M@HA NPs group demonstrated significant inhibition of inflammatory cells infiltration and the disappearance of articular closure or proliferation of the cartilage cells. In addition, obvious IND@PB@M@HA NPs deposition in the synovium further verified its targeting ability. Moreover, IND@PB@M@HA NPs with laser irradiation management group showed a similar smooth cartilage surface without obvious synovial hyperplasia to that of the normal group (Figure 8e). The Bio-Plex suspension chip assay further indicated that the levels of pro-inflammatory factors in the plasma of the model group were significantly higher than that of the normal group. However, the combination of IND@PB@M@HA NPs and photothermal therapy significantly reversed their levels, especially for the IL-1α, IL-2, IL-6, IL-12 and P70 factors (Figure 8f, S6). In addition, heat maps and cluster analysis of inflammatory factors showed that the complete block of IND@PB@M@HA NPs on the RA progression was realised by efficiently reversing the level of inflammatory factors to the normal range (Figure S7).

In vivo *toxicity evaluation*

Finally, the *in vivo* toxicity of IND@PB@M@HA NPs was thoroughly evaluated using different methods. First, the blood routine assay showed the severe inflammatory response in the AIA model rats, which was reflected by the number increase of neutrophils, white blood cells and monocyte. However, all of IND, PB@M@HA NPs and IND@PB@M@HA NPs showed anti-inflammatory function. Among them, IND@PB@M@HA NPs demonstrated the strongest anti-inflammatory effect, as evidenced by the significant reduction of these related factors. In addition, compared with the normal group, blood parameters of red blood cells, platelets, haemoglobin, haematocrit in the rats with different treatments did not show significant changes (Figure 9a).

Hepatic and renal function analyses displayed the decrease of blood urea nitrogen in the IND treatment group, which demonstrated the low protein intake due to the gastrointestinal reaction caused by the IND [41]; however, no similar phenomenon was observed in the IND@PB@M@HA NPs treatment group (Figure 9b). Similarly, H&E staining showed that IND@PB@M@HA NPs did not cause obvious inflammation or systemic toxicity *in vivo* (Figure 9c). In summary, these results showed the high biosafety and biocompatibility of IND@PB@M@HA NPs.

Conclusion

In this study, we report a new targeted drug delivery system to achieve the efficient photo/chemotherapy for RA with an ultra-low dose of IND. As a commonly used anti-inflammatory drug, active ingredient is usually used as a positive control at doses of 1 mg/kg or higher [42]. Compared with pristine active ingredient, the *in vitro* experiments displayed the high targeting ability in the rheumatic joint and low toxicity of PB-based nanocomplexes with a low dos-age of active ingredient. *In vivo* assays demonstrated that the bio-mimetic nanocomplexes can target synovial macrophages through a receptor-ligand recognition system, induce macrophage apop-tosis, inhibit the production of pro-inflammatory cytokines, and accurately deliver drugs. The results of micro-CT and rat ankle joint section analysis indicated that inhibiting the activation of macrophages and reducing the infiltration of inflammatory factors are the main reasons for realising the efficient therapy of RA. Therefore, this combination therapy system with strong anti-inflammatory properties provides a new alternative for the treat-ment of RA.

Author contributions

Shengtao Hu conducted the research, analysed the data, and drafted the manuscript. Ye Lin helped with all of experiments and contributed to data analysis of the draft of the manuscript. Chunyi Tong performed cell culture. Hong Huang and Ouyang Yi performed *in vivo* experiments. Zongshun Dai and Zhaoli Su contributed to data analysis and artwork preparation. Xiong Cai and Bin Liu designed the research, discussed the experiments, analysed the data, and revised the manuscript.

Disclosure statement

The authors declare that they have no conflict of interest.

Funding

References

[1] Smolen JS, Aletaha D, Koeller M, et al. New therapies for treatment of rheumatoid arthritis. Lancet. 2007;370(9602): 1861–1874.

[2] Akter S, Jahan I, Khatun MR, et al. Pharmacological insights into *Merremia vitifolia* (burm.f.) hallier f. leaf for its antioxidant, thrombolytic, anti-arthritic and anti-nociceptive potential. Biosci Rep. 2021;41(1):BSR20203022.

[3] Tan J, Deng Z, Liu G, et al. Anti-inflammatory polymersomes of redox-responsive polyprodug amphiphiles with inflammation-triggered active ingredient release characteris-tics. Biomaterials. 2018;178:608–619.

[4] Crofford LJ. Use of NSAIDs in treating patients with arthritis. Arthritis Res Ther. 2013;15(Suppl 3):S2.

[5] Littlejohn EA, Monrad SU. Early diagnosis and treatment of rheumatoid arthritis. Prim Care. 2018;45(2):237–255.

[6] Feng X, Liu J, Xu W, et al. Tackling autoimmunity with nanomedicines. Nanomedicine. 2020;15(16):1585–1597.

[7] Feng X, Xu W, Li Z, et al. Immunomodulatory nanosystems. Adv Sci. 2019;6(17):1900101.

[8] Gadeval A, Chaudhari S, Bollampally SP, et al. Integrated nanomaterials for non-invasive photothermal therapy of rheumatoid arthritis. Drug Discov Today. 2021;26(10): 2315–2328.

[9] Lu Y, Li L, Lin Z, et al. A new treatment modality for rheumatoid arthritis: combined photothermal and photodynamic therapy using Cu7.2 S4 nanoparticles. Adv Healthc Mater. 2018;7(14):e1800013.

[10] Gao Y, Yu G, Xing K, et al. Finely tuned Prussian blue-based nanoparticles and their application in disease treatment. J Mater Chem B. 2020;8(32):7121–7134.

[11] Zhang S, Wu L, Cao J, et al. Effect of magnetic nanoparticles size on rheumatoid arthritis targeting and photothermal therapy. Colloids Surf B Biointerfaces. 2018;170: 224–232.

[12] Sahu A, Jeon J, Lee MS, et al. Antioxidant and anti-inflammatory activities of Prussian blue nanozyme promotes full-thickness skin wound healing. Mater Sci Eng C Mater Biol Appl. 2021;119:111596.

[13] Cai X, Gao W, Ma M, et al. A Prussian blue-based core-shell hollow-structured mesoporous nanoparticle as a smart theranostic agent with ultrahigh pH-Responsive longitudinal relaxivity. Adv Mater. 2015;27(41):6382–6389.

[14] Liu B, Wang W, Fan J, et al. RBC membrane camouflaged Prussian blue nanoparticles for gamabutolin loading and combined chemo/photothermal therapy of breast cancer. Biomaterials. 2019;217:119301.

[15] Fang RH, Kroll AV, Gao W, et al. Cell membrane coating nanotechnology. Adv Mater. 2018;30(23):e1706759.

[16] Liu Y, Luo J, Chen X, et al. Cell membrane coating technology: a promising strategy for biomedical applications. Nanomicro Lett. 2019;11(1):100.

[17] Long Y, Wang Z, Fan J, et al. A hybrid membrane coating nanodrug system against gastric cancer via the VEGFR2/STAT3 signaling pathway. J Mater Chem B. 2021;9(18): 3838–3855.

[18] Hou M, Wei Y, Zhao Z, et al. Immuno-engineered nanodecoys for the multi-target anti-inflammatory treatment of autoimmune diseases. Adv Mater. 2022;:e2108817. doi:10.1002/adma.202108817.

[19] Li R, He Y, Zhu Y, et al. Route to rheumatoid arthritis by macrophage-derived microvesicle-coated nanoparticles. Nano Lett. 2019;19(1):124–134.

[20] Zhou M, Hou J, Zhong Z, et al. Targeted delivery of hyaluronic acid-coated solid lipid nanoparticles for rheumatoid arthritis therapy. Drug Deliv. 2018;25(1):716–722.

[21] Liu Y, Jin J, Xu H, et al. Construction of a pH-responsive, ultralow-dose triptolide nanomedicine for safe rheumatoid arthritis therapy. Acta Biomater. 2021;121:541–553.

[22] Zhou H, You P, Liu H, et al. Artemisinin and procyanidins loaded multifunctional nanocomplexes alleviate atherosclerosis via simultaneously modulating lipid influx and cholesterol efflux. J Control Release. 2022;341:828–843.

[23] Jiang Q, Liu Y, Guo R, et al. Erythrocyte-cancer hybrid membrane-camouflaged melanin nanoparticles for enhancing photothermal therapy efficacy in tumors. Biomaterials. 2019;192:292–308.

[24] Wang D, Dong H, Li M, et al. Erythrocyte-cancer hybrid membrane camouflaged hollow copper sulfide nanoparticles for prolonged circulation life and homotypic-targeting photothermal/chemotherapy of melanoma. ACS Nano. 2018;12(6):5241–5252.

[25] Zhang X, Servos MR, Liu J. Fast pH-assisted functionalization of silver nanoparticles with monothiolated DNA. Chem Commun. 2012;48(81):10114–10116.

[26] Cai X, Wong YF, Zhou H, et al. The comparative study of Sprague-Dawley and Lewis rats in adjuvant-induced arthritis. Naunyn Schmiedebergs Arch Pharmacol. 2006;373(2): 140–147.

[27] Belmellat N, Semerano L, Segueni N, et al. Tumor necrosis factor-alpha targeting can protect against arthritis with low sensitization to infection. Front Immunol. 2017;8:1533.

[28] Levick JR. Hypoxia and acidosis in chronic inflammatory arthritis; relation to vascular supply and dynamic effusion pressure. J Rheumatol. 1990;17(5):579–582.

[29] Siniavin AE, Streltsova MA, Kudryavtsev DS, et al. Activation of α7 nicotinic acetylcholine receptor upregulates HLA-DR and macrophage receptors: potential role in adaptive immunity and in preventing immunosuppression. Biomolecules. 2020;10(4):507.

[30] Rao L, Wu L, Liu Z, et al. Hybrid cellular membrane nanovesicles amplify macrophage immune responses against cancer recurrence and metastasis. Nat Commun. 2020;11(1): 4909.

[31] Gholibegloo E, Karbasi A, Pourhajibagher M, et al. Carnosine-graphene oxide conjugates decorated with hydroxyapatite as promising nanocarrier for ICG loading with enhanced antibacterial effects in photodynamic therapy against *Streptococcus mutans*. J. Photochem. Photobiol. B Biol. 2018;181:14–22.

[32] Li ZH, Chen Y, Sun Y, et al. Platinum-Doped Prussian blue nanozymes for multiwavelength bioimaging guided photothermal therapy of tumor and anti-Inflammation. ACS Nano. 2021;15(3):5189–5200.

[33] Xie X, Zhao J, Gao W, et al. Prussian blue nanozyme-mediated nanoscavenger ameliorates acute pancreatitis via inhibiting TLRs/NF-κB signaling pathway. Theranostics. 2021;11(7):3213–3228.

[34] Long Y, Wu X, Li Z, et al. PEGylated WS2 nanodrug system with erythrocyte membrane coating for chemo/photothermal therapy of cervical cancer. Biomater Sci. 2020;8(18): 5088–5105.

[35] Kang H, Hu S, Cho MH, et al. Theranostic nanosystems for targeted cancer therapy. Nano Today. 2018;23:59–72.

[36] Xue W, Liu Y, Zhang N, et al. Effects of core size and PEG coating layer of iron oxide nanoparticles on the distribution and metabolism in mice. Int J Nanomed. 2018;13: 5719–5731.

[37] Yang Y, Guo L, Wang Z, et al. Targeted silver nanoparticles for rheumatoid arthritis therapy via macrophage apoptosis and re-polarization. Biomaterials. 2021;264: 120390.

[38] Tabas I, Glass CK. Anti-inflammatory therapy in chronic disease: challenges and opportunities. Science. 2013; 339(6116):166–172.

[39] Khojah HM, Ahmed S, Abdel-Rahman MS, et al. Reactive oxygen and nitrogen species in patients with rheumatoid arthritis as potential biomarkers for disease activity and the role of antioxidants. Free Radic Biol Med. 2016;97:285–291.

[40] Jiulong Z, Xiaojun C, Wei G, et al. Prussian blue nanozyme with multienzyme activity reduces colitis in mice. ACS Appl Mater Interfaces. 2018;10(31):26108–26117.

[41] Suzuki S, Kokumai T, Tanahashi Y, et al. Protein ingestion can significantly affect glucagon secretion along with blood urea nitrogen alteration in type 1 diabetes. J Diabetes Investig. 2021;12(2):293–294.

[42] Ahmed EA, Ahmed OM, Fahim HI, et al. Potency of bone marrow-derived mesenchymal stem cells and active ingredient in complete Freund's adjuvant-induced arthritic rats: roles of TNF-α, IL-10, iNOS, MMP-9, and TGF-β1. Stem Cells Int. 2021;2021:6665601.